A novel approach for the fabrication of carbon nanofibre/ceramic porous structures

Claudia Walter [a,*], Suelen Barg [a], Na Ni [a], Robert C. Maher [b], Esther García-Tuñón [a], Muhammad Muzzafar Zaiviji Ismail [a], Flora Babot [a], Eduardo Saiz [a]

[a] *Centre for Advanced Structural Ceramics, Department of Materials, Imperial College London, London SW7 2AZ, United Kingdom*
[b] *Department of Physics, Imperial College London, London SW7 2AZ, United Kingdom*

Introduction

Carbon nanotubes (CNTs) and nanofibres have a set of desirable properties but their incorporation into structural parts is often still a challenge. Their unique mechanical, electrical and chemical properties open new opportunities in a wide range of technologies.[1,2] They have been investigated as reinforcement in ceramic materials,[3–10] to build tissue engineering scaffolds[11–13] water-cleaning filters[14] or as electrodes in fuel cells or batteries[15,16] to name a few applications. In many of these cases the challenge is their incorporation into stable three-dimensional structures optimized for the specific use. This is often a complex problem, as it requires the simultaneous manipulation of their distribution at the micro-scale and the overall structure at the micro to macro-levels. For example, many of these applications (e.g. tissue engineering scaffolds or fuel cells) require the combination of macroporosity to facilitate transport, high surface area and mechanical stability. These requirements are often contradictory (like the combination of macroporosity and mechanical strength) and demand new approaches to design and build structures.

Several techniques have been proposed for the fabrication of porous CNT or nanofibre-based structures, these include emulsion templating where the CNTs are used to stabilize polymer based emulsions,[17] electrophoretic deposition to cover the walls of porous glass scaffolds,[18] freeze casting of CNT suspensions,[15] electrospinning,[19] or use of composite powders[20] to name a few. From the processing point of view wet approaches are very versatile and easily scalable; however, they face difficulties associated with the preparation of concentrated suspensions containing carbon nanostructures with the required properties. As an alternative, the in situ growth of nanotubes and fibres inside porous ceramic foams has also been investigated. In most cases chemical vapor deposition and/or metallic catalysts are used to promote CNT or nanofibre formation.[21–23] Here the issue is to control the catalyst distribution and gas flow inside the porous structure in a way that growth can be achieved in pores of decreasing size.

* Corresponding author. Present address: Department of Materials Science and Metallurgy, University of Cambridge, Pembroke Street, Cambridge CB2 3QZ, United Kingdom. Tel.: +44 1223 334300; fax: +44 1223 334567.
E-mail address: cwalter@gmx.com (C. Walter).

In this paper we describe the growth of carbon nanofibres and multi-walled nanotubes covering the internal walls of freeze casted lamellar alumina scaffolds. Freeze casting is used to build porous Al_2O_3 scaffolds with directional porosity of controlled width. This ceramic support provides mechanical stability to the structure. Subsequently, a two-step chemical vapor deposition process based on the infiltration of a catalyst precursor followed by a thermal treatment is used to grow the fibres and nanotubes inside the scaffold. The formation of the scaffold structure and its role on the process (in particular the role of pore size) are investigated to define the growth conditions (precursor concentration, temperature and atmosphere) leading to a porous ceramic scaffold whose internal walls are fully covered.

Experimental procedure

Ceramic scaffolds

The freeze caster for the preparation of ceramic scaffolds with lamellar porosity using the directional freezing of ceramic suspensions was built in-house. The centre piece for freezing of the ceramic suspensions is a cylindrical mould with an inner diameter of 20 mm. To guide the heat flow from the bottom to the top of the mould the walls are made of insulating Teflon® while the bottom plate is made of very conductive copper and sits on a copper cold finger. The temperature at the top of the copper cold finger right underneath the mould can be lowered down to −100 °C at controlled rates of up to 15 K/min. Temperature control is achieved through a liquid nitrogen bath and a ring heater run by a controller connected to a thermocouple at the top of the cold finger.

Suspensions were prepared with solid loadings between 20 and 50 wt% of alumina powder with an average particle size of 300 nm (Baikalox SMA 6). The powder was dispersed in distilled water with the addition of 1.4 wt% Dolapix CA as electrosteric dispersant agent and 1.4 wt% of polyvinylalcohol as the binder (both related to the total alumina weight). Further on, 4 wt% sucrose with regards to suspension water content is added to the suspensions.[24] All suspensions were ball milled for at least 12 h. Air bubbles were removed from the suspensions by stirring under vacuum. The suspensions were then directionally frozen in the freeze caster and transferred to the freeze drier in order to sublimate the ice and leave a ceramic scaffold green body.

The green bodies were sintered in air at a temperature of 1550 °C for 2 h to produce the final alumina scaffolds. The scaffolds were ground to a height of approximately 10 mm, removing a layer of dense material that forms at the bottom of the mould[24] and thus ensuring open porosity for subsequent infiltration and CNT growth. Potential carbon residue from the diamond grinding disc was removed by a 1 h heat treatment at 1200 °C in air.

Composites

The general methodology used for the preparation of composites is shown in Fig. 1. The first step is the preparation of the alumina lamellar scaffolds (as described in previous section). This is followed by infiltration with a catalyst precursor and the chemical vapour deposition process which includes reduction/formation of the metallic catalyst particles and CNT and nanofibre growth. In this work, iron and nickel were chosen as catalysts and the alumina scaffolds were infiltrated with a 1.1 M solution of Iron(III)nitrate nonahydrate or nickel(II)nitrate hexahydrate in iso-propanol.[25] To achieve good penetration of the solution into the scaffolds standard vacuum infiltration equipment was used (Buehler Cast N' Vac). Afterwards the solvent was removed at 60 °C under vacuum.

For the chemical vapour deposition process the infiltrated sample was placed inside a quartz tube furnace (Ø 33 mm) and the system was purged with a gas mixture of 90% argon and 10% hydrogen for 30 min at a flow rate of 0.5 l/min. All gas flows are at 1 bar and measured in l/min as calibrated for air. Then the sample was heated at maximum rate (∼1 K/s) to the growth temperature (between 700 °C and 900 °C). The presence of hydrogen leads to a reduction of the catalyst compound to pure iron particles during this process. Upon reaching the desired growth temperature methane was added to the gas mixture. Growth time was 20 min after which the methane supply was closed and the sample was left inside the furnace to cool down to room temperature in argon–hydrogen atmosphere. Water and ethanol were tested as growth enhancers. They were added by passing defined amounts of either the methane or the argon–hydrogen gas through a wash bottle with the enhancer before entering the quartz tube furnace during the 20 min growth time.

The microstructure and composition of the scaffolds and composites was investigated using scanning and transmission electron microscopies, X-ray diffraction and Raman spectroscopy. In order to measure the lamella and pore size of the scaffolds after sintering, the scaffolds were embedded in epoxy resin and cross sections were prepared and polished for imaging in the scanning electron microscope. For each sample 4

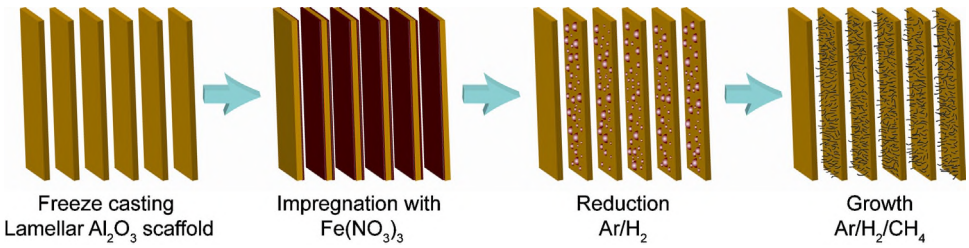

Fig. 1. Schematic of the processing route. The key steps are the fabrication of the porous lamellar scaffold, the formation of the catalyst particles and the growth of the carbon nanostructures inside the confined porosity.

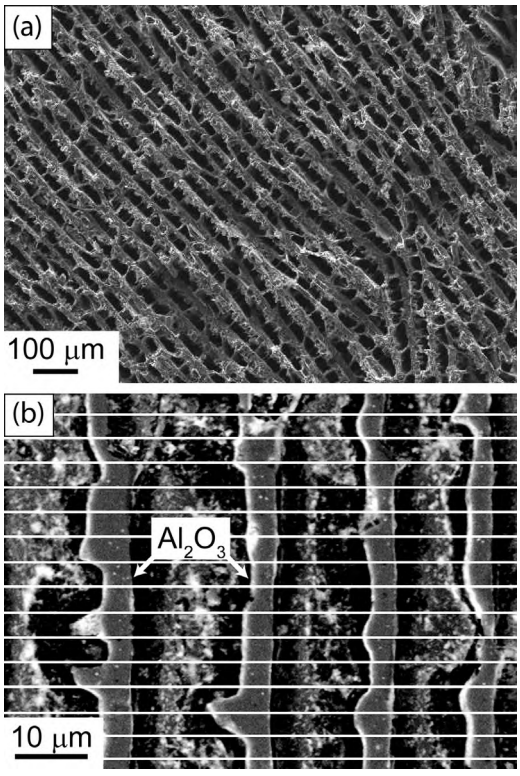

Fig. 2. SEM images of the alumina scaffolds: (a) fracture surface of a scaffold at lower magnification in a plane perpendicular to the direction of ice growth and (b) polished scaffold embedded in resin showing four ceramic lamellae at magnification used for analysis. White lines indicate the fixed grid used for the measurement of lamellae and pore size.

images were taken at different locations within the cross section, each image containing 2–4 lamellae for measurement. A fixed grid of 16 lines of measurement for the sizes and spacing was placed across each image (Fig. 2) resulting in 100–200 data points for lamella size and spacing per sample. Transmission electron microscopy (TEM) was carried out on a FEI Titan 80-300S/TEM operated at 300 kV, equipped with a monochromator and a Cs aberration image corrector. The TEM specimens were prepared by dispersing small flakes of the hybrid material in acetone and drop casting them on carbon coated TEM copper grids. All Raman measurements were performed using a Renishaw RM2000 CCD spectrometer equipped with a 514 nm laser. The laser was focused onto the sample using a 50× short working distance objective resulting in a spot of approximately 1.5 μm diameter. A laser power 0.5 mW at the focal point was used with an integration time of 10 s to ensure good signal to noise ratios. Several spectra were collected from random locations on each sample.

FE modelling

As the structure of the freeze casted material depends to a large extent on the speed and direction of the freezing front, finite element modelling was used to visualize the development of the temperature gradient in the suspensions during freezing. Exploiting the rotational symmetry of the cylindrical set-up, a slice from the centre to the outside was modelled. It includes the

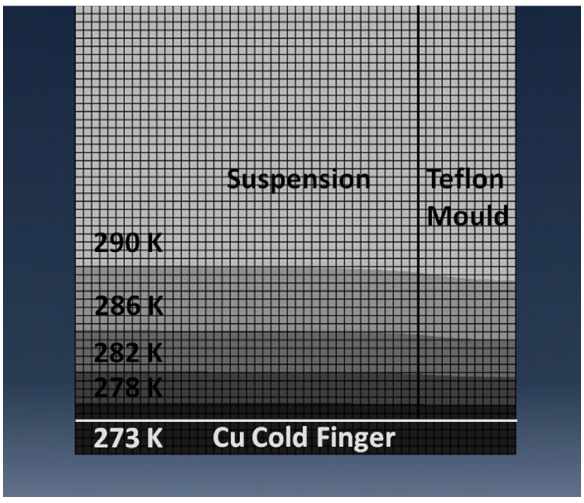

Fig. 3. FE simulation of the temperature gradient in the freeze casting set-up. A slice through the cylindrical mould from the centre (left) to the outside (right) is shown. Contour bands indicate the temperature in steps of 5 K.

Teflon wall of the mould, the copper cold finger, and the sample inside the mould. The material properties used for the simulation are listed in Table 1. The sample is assumed to be water/ice and heat exchange between the set-up and the environment is neglected. Despite these simplifications the simulation should be able to provide a general idea of the evolution of the temperature gradient up to the point when freezing starts. At the start of a simulation the temperature of the entire model is set to 293 K. Subsequently, the temperature of all elements in the copper cold finger is lowered at a rate of 5 K/min, thus imitating a freeze casting experiment run at a cooling rate of 5 K/min.

Results and discussion

Ceramic scaffolds

Fig. 3 shows the simulated temperatures in the set-up at the point when the cold finger reaches the freezing temperature of the sample (273 K). A clear temperature gradient from the bottom to the top of the sample can be observed. Across the sample the temperature is constant dropping off only to a small extent across the Teflon mould walls. Thus the conditions for directional solidification are good and a planar freezing front can be expected to move through the samples. These simulations are only applied as a rough guide to the conditions inside the set-up. The actual speed of the freezing front for all suspensions was measured experimentally as described in the next paragraph.

In a first series of experiments a transparent mould made of Perspex was used to observe the advancing ice-front and relate the cooling rate at the top of the cold finger to a freezing speed (meaning the speed of the ice-front) inside the ceramic suspension. Fig. 4 shows the freezing speed at cooling rates of 1, 5, 10, and 15 K/min for suspensions with different solid loading. Freezing speeds ranging from 8 to 48 μm/s were observed. The freezing speed increases approximately linearly with increasing cooling rate. An influence of the solid loading could not be detected even though it would be anticipated due to differences

Table 1
Material parameters used in the finite element model.

	Density (kg/m^3)	Specific heat (J/kg K)	Thermal conductivity (W/m K)	Latent heat of fusion (kJ/kg)
Teflon mould	2160	1010	0.23	–
Copper cold finger	8940	390	401	–
Water/ice	1000/910	4200/2100	0.59/2.22	334

in the thermal conductivities of the ceramic particles and the surrounding water. Most likely this effect could not be captured within the accuracy of measurement. The freezing speed was measured at intervals until the freezing front reached a distance of 20 mm from the cold finger and was observed to be constant over this distance.

During directional freezing the speed of the freezing front greatly influences the developing microstructure.[24] For conditions under which a lamellar structure develops the freezing speed can be used to tune the size of the lamellae and pores. Increasing speed generally leads to a finer structure.[26] This effect was investigated for the set of suspensions and freezing conditions shown in Fig. 4. The average lamella thickness and pore widths and their standard deviation as a function of the freezing speed and solid loading are shown in Fig. 5a and b. Fig. 5a shows clearly how the thickness of the lamellae is decreasing with increasing speed of the freezing front. For example, changing the speed from 10 to 45 μm/s decreases the lamella thickness from 13 to 4 μm for a suspension with 40% solid loading. This trend is observed for all solid loadings and this is in general agreement with the literature.[26,27] Focussing on one constant freezing speed, a higher solid loading will lead to thicker lamellae. At a speed of approximately 10 μm/s the lamella width will range from 5 μm for 20% solid loading to 18 μm for 50% solid loading. Suspensions with solid loading higher than 50% or lower than 20% will either not yield lamellar structures because they are too concentrated or produce mechanically unstable green bodies due to lack of solid material.[24,28] The measured lamella thicknesses for the slurry with 50% solid loading are in excellent agreement with experiments by Deville et al. for a comparable slurry and set-up.[26] Overall, these experimental conditions allow for tuning of the thickness of the lamellae over one order of magnitude between 2 and 20 μm.

In analogy to the lamella thickness, the pore width shown in Fig. 5b tends to decrease at higher freezing speed. Overall, the measured pore widths range between 11 and 63 μm. For freezing front speeds >15 μm/s the lamella spacing decreases from a value of around 30–15 μm without a significant influence of the solid loading. At low freezing speeds the scatter within each sample and between the different solid loadings becomes large. This is in agreement with the general observation that a power law governs the correlation between the structural wavelength (defined as the average size of one structural unit which contains one lamella and one pore) and the freezing front speed (Fig. 6) and, therefore, at slow freezing speeds small changes in the freezing speed can produce large changes in the structure. Focussing on one constant freezing speed, pore widths tend to be smaller for higher solid loading. Generally, the solid loading becomes apparent as a limiting factor for the pore width which reaches an upper limit of approximately 30 μm for the

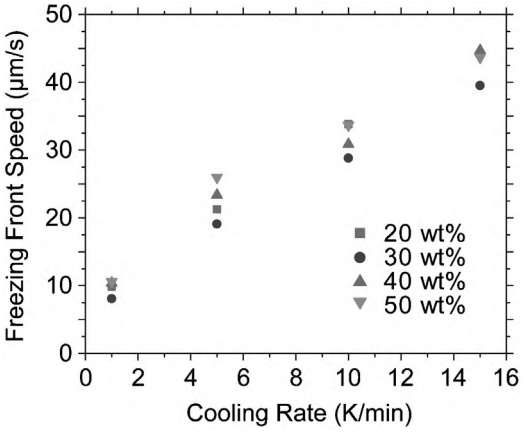

Fig. 4. Speed of the freezing front in suspensions with different solid loading as a function of the cooling rate of the equipment cold finger. The dependence is practically linear in the range of conditions used in this work.

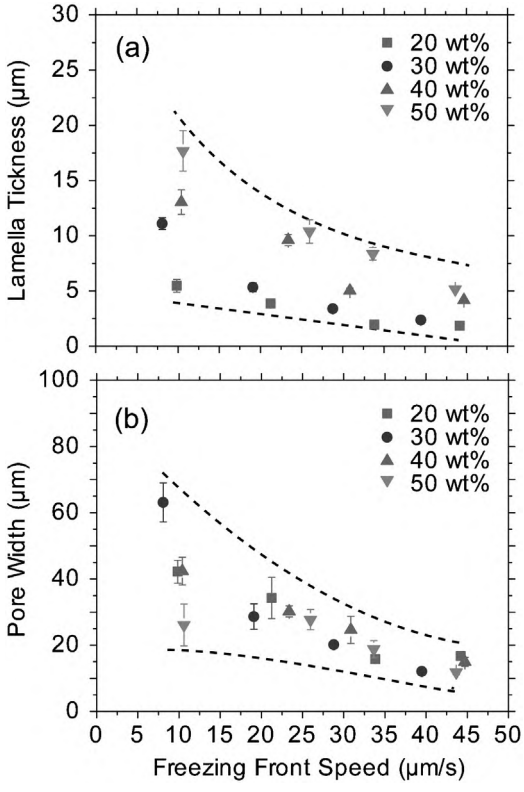

Fig. 5. Dependence of the (a) lamella thickness and (b) pore width of freeze casted Al_2O_3 structures with the speed of the freezing front in the suspensions. The ranges of structural dimensions accessible within the experimental conditions are bounded by dotted lines.

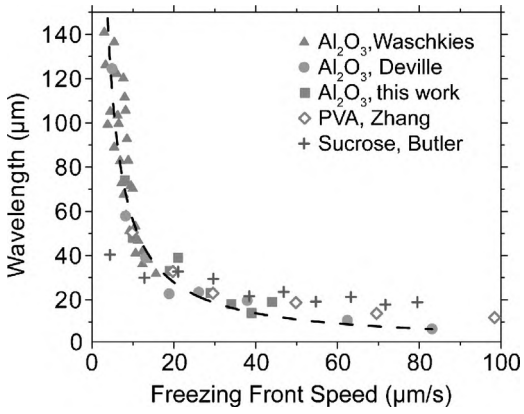

Fig. 6. Wavelength of freeze casted lamellar structures as a function of the freezing front speed for Al_2O_3 suspensions (Waschkies,[27] Deville,[24] our data) and particle free suspensions (Zhang,[30] Butler [29]). The dotted line shows the fit of a power law with a coefficient of −1 to all Al_2O_3 data.

highest solid loading towards the slower freezing speeds and a lower limit of approximately 15 μm for the lowest solid loading towards the faster freezing speeds. Overall, a variation in pore width between 10 and 90 μm seems achievable as indicated by the dotted lines in Fig. 5b.

In the literature, a power law dependence between the freezing speed and the structural wavelength of freeze casted suspensions has been proposed.[24] Deville et al. reported a power law exponent value of −1 for an alumina suspension with 0.4 μm particle size.[24] Waschkies et al. fitted a simple power law to the spacing as a function of the freezing speed and reported exponent values between −0.8 and −1.3 for alumina slurries with a range of solid loadings and a particle size of 0.8 μm.[27]

Our data provides four data points at different freezing speeds per solid loading which is insufficient for a good quality power law fit. However, our data for 20 wt% and 30 wt% solid loading appears to be consistent with a general power law when plotted with literature values as shown in Fig. 6. It should be mentioned that Deville's and our data has been measured after sintering while other data was collected in the frozen state[27,29] or after freeze drying.[30] Sintering could have caused the structure to shrink but deviations in the wavelength of up to 10% would still give a reasonable fit to the proposed power law. The power law fit with an exponent value of −1 as suggested in the literature is shown as a dashed line. Also shown are two sets of data for particle free suspensions: Zhang et al. froze a suspension of 5 wt% PVA in water[30] and Butler froze a solution of 5% sucrose in water.[29]

While the data for the PVA solution seems to agree well with the established power law, the sucrose solution data deviates at low freezing speeds. However, it must be pointed out that the experimental conditions for the sucrose experiment and the other papers are different. In all the other papers the temperature of the bottom surface decreases with time and the resulting temperature gradient across the sample is not constant with time (as it can be seen both experimentally and in the simulations). The speed of the freezing front is manipulated by varying the speed at which the gradient changes (or the cooling rate of the bottom surface). In the sucrose experiment, like in many other basic studies of solidification, the sample is displaced in a constant temperature gradient at different speeds in order to vary the speed of the solidification front. In this case the dendrite primary spacing (λ) is described in terms of the temperature gradient (G) and the growth velocity (v) using the expression, $\lambda = AG^{-1/2}v^{-1/4}$. However, a general observation is that both experimental set-ups seem to give similar results at higher freezing speeds. Similarly, for relatively low content of ceramic particles (<30 wt%) the ceramic suspensions appear to show similar behaviour to particle free solutions at freezing speeds exceeding 10 μm/s. Suspensions with a higher solid loading of 40 wt% and 50 wt% started to deviate from this trend. It can only be suspected that at these higher concentrations the influence of the particles on the freezing behaviour increases through e.g., particle–particle interactions, modifications of the temperature gradient or pressure on the ice crystals.

Overall, the freeze casting method allows for the preparation of layered ceramic structures of tangible sizes with layer thicknesses between 2 and 20 μm in a relatively simple and efficient way. The pore size is large enough for easy infiltration of the catalyst precursor solution for CNT and nanofibre growth and preparation of composites.

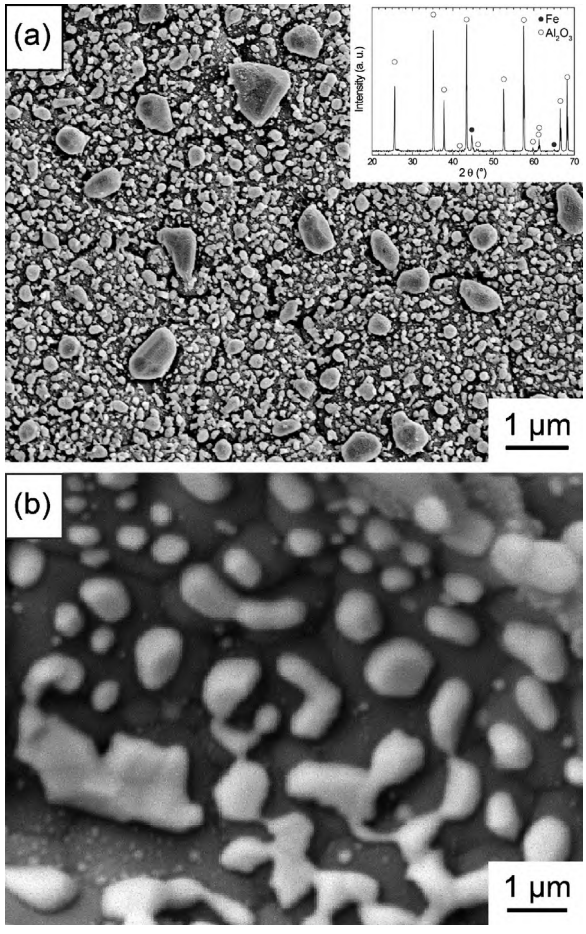

Fig. 7. Coverage of the internal alumina scaffold surfaces with iron catalyst particles after reduction at (a) 800 °C, identification of the particles as Fe by XRD shown in the inset, and (b) 900 °C. Significant coarsening is observed in the samples reduced at higher temperature.

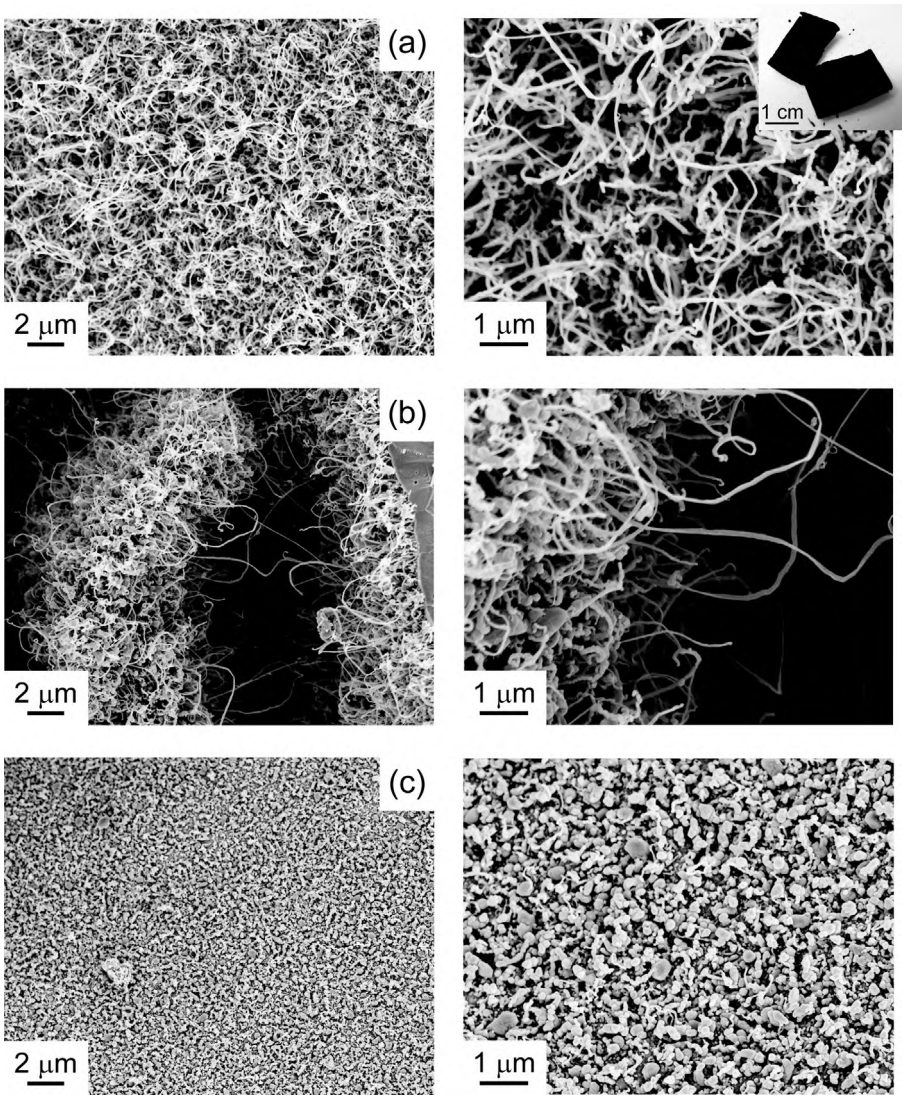

Fig. 8. SEM micrographs of the interior walls of the alumina structures after CNT/nanofibre growth with (a, top row) 0.2 l/min methane, no enhancer, (b, centre row) 0.4 l/min methane total of which 0.2 l/min methane passed through enhancer, and (c, bottom row) 0.8 l/min methane total of which 0.4 l/min methane passed through enhancer. The inset in (a) shows homogenous coverage in the interior of the Al_2O_3 scaffolds (revealed after breaking the scaffold in 2 pieces).

Composites

In a next step the feasibility of in situ growth of nanotubes and nanofibres within the ceramic scaffolds was tested. Successful growth by chemical vapour deposition depends on the interplay of a number of processing parameters such as choice and distribution of catalyst, carbon source, growth temperature, and gas flows. The growth conditions chosen here are based on published methods for the growth of CNTs on ceramics.[21,22,25] Optimization of the process parameters for our ceramic scaffolds is necessary to achieve growth inside the confined microporosity.

As a first step towards chemical vapour deposition (CVD) growth the scaffolds need to be impregnated with a suitable catalyst. This was done by vacuum infiltration with a solution of iron(III)nitrate nonahydrate dissolved in iso-propanol. Solutions with different molarities of iron(III)nitrate were tested from 50 mM to 1.1 M which was the highest amount that could be easily dissolved before the iron started oxidizing while dissolving. The reduction of the infiltrated iron compound to pure iron nanoparticles was inspected by heating the sample to the growth temperature (between 700 °C and 900 °C) in argon–hydrogen atmosphere and immediately cooling back down. The high contact angle of Fe on Al_2O_3 (>90 ° in reducing atmospheres) promotes the formation of small, "non-wetting" catalyst particles on the internal walls of the scaffold.[31] The solution with the highest molarity (1.1 M) resulted in the densest coverage of the scaffolds with catalyst particles with submicron size that provided the highest yield of nanofibres and CNTs. Differences between the samples could easily be resolved by visual inspection in the SEM. Fig. 7a shows the distribution of iron catalyst particles on an internal surface of the alumina scaffold for a 1.1 M solution at 800 °C. The presence of iron in elemental form could be shown by X-ray diffraction (see inset Fig. 7a). With the current preparation steps a significant amount of iron catalyst can be expected to remain in the final composite. A simple estimation based on the relative pore volume and the

concentration of the precursor suggest that the content is of the order of 1–2 wt% which seems consistent with the relative height of the XRD peaks (Fig. 7a). Although in some cases the presence of isolated metallic particles may not have an effect on the performance of the material, some applications may require the elimination of the catalyst (for example, it can be detrimental when using at high temperatures where iron diffusion could be an issue). In that case, methods such as acid washing or high temperature annealing would have to be applied at a later stage in order to remove the iron from the composite.[32–34]

Nickel is mentioned as an alternative catalyst in the literature. Thus, the experiments were repeated using nickel(II)nitrate hexahydrate. However, no growth was observed using the nickel catalyst in our set-up.

A series of growth experiments was conducted varying the growth temperature between 700 °C and 90 °C in steps of 50 °C while maintaining all other process parameters constant as follows: 0.5 l/min argon–hydrogen, 0.2 l/min methane, growth time 20 min. The highest yield was achieved at a temperature of 800 °C which was used for all further experiments. At higher temperatures the catalyst particles started to coarsen significantly as shown in Fig. 7b for 900 °C and this inhibits growth. Fig. 8a shows the coverage achieved at 800 °C. The micrograph is taken on the inside of a scaffold with an average pore width of 70 μm. The inset (top right corner) shows how the entire alumina scaffold is homogeneously coated.

The TEM analysis reveals the organization of nanofibres and nanotubes inside the scaffold (Fig. 9). Nanofibres grow from and bundle around the catalyst particles deposited on the ceramic walls while multi-walled nanotubes grow from the catalyst covered walls into the pores. No evidence for amorphous carbon covering the catalyst particles is observed. The tubes have a small catalyst particle on top. This picture agrees with existing models of nanotube growth in which multi-wall CNTs grow from small catalytic particles that can rest on a larger one that acts as a support while the smaller one is "lifted" by the growth of the nanotube.[35] The distribution of nanotubes and nanofibres probably reflect the distribution of sizes of the catalyst particles formed after infiltration.[36,37]

Recent reports in the literature state that the addition of an oxygen source, such as water or ethanol, to the growth process can significantly enhance CNT growth.[38–40] It is believed that the oxygen thus added to the process activates the catalyst by removing amorphous carbon coatings and inhibiting Oswald

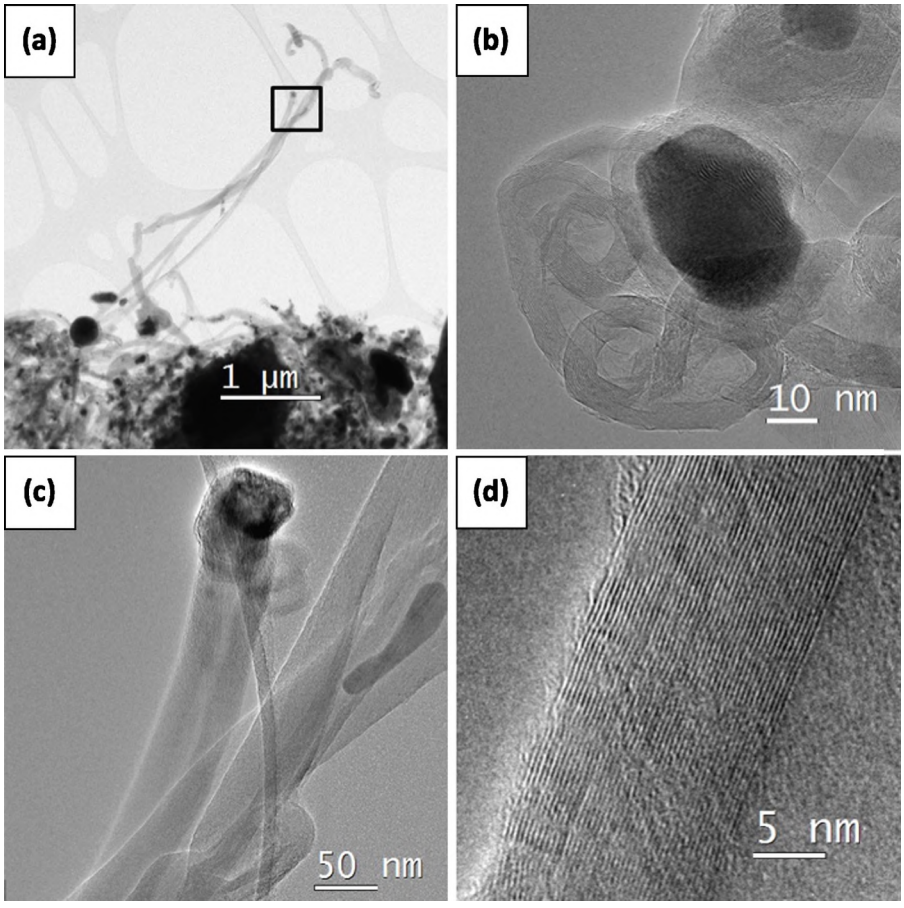

Fig. 9. Transmission electron micrographs of the samples after growth showing the nanofibres and multi-walled CNTs. (a) Low magnification TEM of the hybrid material, showing the presence of different carbon nanostructures. Fe catalyst particles appear dark in the image. Nanofibres grow and bundle around the catalyst particle with several μm long multi-walled CNTs growing from the catalyst particle towards the pore. (b) Typical nanofibres growing from a Fe catalyst particle. (c) Enlarged image of the area indicated in (a) with the box, showing a multi-walled CNT growing from a Fe particle with a small catalyst particle on top. A high-resolution image of the left wall of the CNT in (c) is shown in (d).

ripening of the catalyst.[38,40,41] Thus, a few experiments were conducted to see if the addition of water or ethanol to the process could boost growth within the scaffolds even further. Therefore, part of the methane gas was passed through wash bottles filled with 60 ml of enhancer, here ethanol, before entering the furnace. The flow of the argon–hydrogen mixture remained unchanged at 0.5 l/min. A series of four experiments with the following gas flow combination was run:

(1) 0.2 l/min methane total, no enhancer (Fig. 8a).
(2) 0.4 l/min methane total, of which 0.2 l/min methane passed through enhancer (Fig. 8b).
(3) 0.4 l/min methane total, no enhancer.
(4) 0.8 l/min methane total, of which 0.4 l/min methane passed through enhancer (Fig. 8c).

Compared to experiment 1, representing the standard conditions without any enhancer (Fig. 8a), only experiment 2 gave similar results in terms of growth (Fig. 8b). Experiments 3 and 4 yielded significantly less CNTs and nanofibres as shown in Fig. 8c for experiment 4. Thus, neither the enhancer nor an increase in methane flow could produce a significantly higher yield than the original growth conditions with 0.2 l/min methane and no enhancer. A quantification of the amount of nanotube and fibre grown was attempted by thermogravimetric analysis but mass gain due to oxidation of the catalyst overlays the mass loss due to combustion of carbon and makes quantification difficult.

The same set of experiments was conducted using water instead of ethanol as the enhancer. Within the tested conditions CNT and nanofibre growth was significantly diminished or completely absent when water was added to the process. In this study no setting could be found to use the enhancers effectively for the in situ growth. A detailed study by Futaba and co-workers showed that results depend critically on finding the optimum quantity of enhancer in combination with the carbon source used.[38] The flow conditions within the scaffold may be such that the fine balance needed between enhancer and carbon source could not be established. A more detailed study of the flow conditions inside the scaffold and their influence on the growth process would be of great interest here but is outside the scope of this manuscript.

Last, a rough estimate of the effect of the pore size on the process was attempted. Experiments 1–4 were repeated using a scaffold with a larger pore size of 87 μm, and a scaffold with a smaller pore size of 27 μm. For the larger pore size the yield and the trend concerning the influence of the enhancer were in good agreement with the results achieved for the scaffold with 70 μm pore size. For the scaffold with the smaller pore size no homogeneous coverage could be achieved under the tested conditions. Thus, the critical pore size below which the flow conditions have a detrimental effect on this method lies somewhere between 70 μm and 27 μm.

Raman spectroscopy was used to assess the quality of the CNTs and fibres grown inside the alumina scaffolds. *D*/*G* ratios for three samples where growth was quite effective are shown in Table 2. These ratios are all low reflecting the highly graphitic quality, and low defect nature of the carbon formed. The ratios also emphasize and reflect the difference observed in the averaged spectra shown in Fig. 10. The larger 0.18 ratio observed for the 0.2 l/min methane through ethanol in 70 μm pore spectrum indicates that it is slightly more defective.

Table 2
D/*G* ratio of CNTs with different growth conditions.

	Pore size (μm)	*D* peak	*G* peak	*D*/*G* ratio
0.2 l/min methane	87	922	6261	0.15
0.4 l/min methane total with 0.2 l/min through ethanol	87	822	6197	0.13
0.4 l/min methane total with 0.2 l/min through ethanol	70	876	4872	0.18

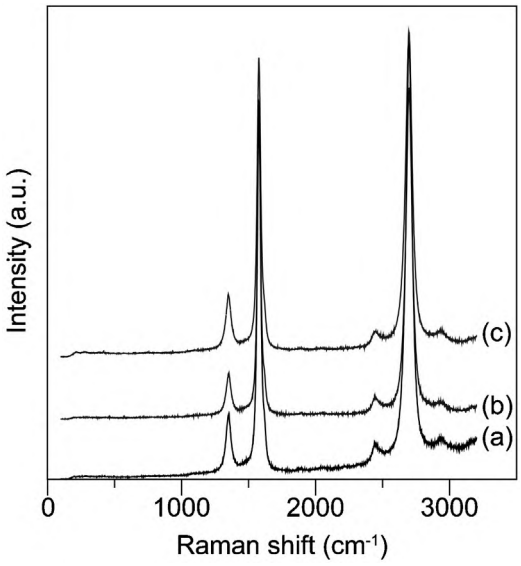

Fig. 10. Raman spectra (averaged from different regions of each sample) of composite structures containing high amounts of CNTs/nanofibres homogeneously distributed. (a) 0.2 l/min methane total, 87 μm pore size scaffold; (b) 0.4 l/min methane total of which 0.2 l/min methane passes through ethanol, 87 μm pore size scaffold; (c) 0.4 l/min methane total of which 0.2 l/min methane passes through ethanol, 70 μm pore size scaffold.

Summary

In summary, a method was developed for the fabrication of ceramic/carbon nanofibre scaffolds involving the infiltration of a ceramic scaffold with a suitable catalyst precursor followed by thermal treatments under controlled atmospheres containing a carbon source. First, alumina scaffolds were produced by directional freezing at cooling rates between 1 and 15 K/min. These scaffolds have a porous lamellar structure whose wavelength can be manipulated by controlling the freezing speed and the solid loading of the starting suspensions. As a result, the ceramic layer thickness can be controlled over an order of magnitude in the range between 2 and 20 μm. The pore size could be varied between 10 and 90 μm allowing an exploration of the role of pore

size. Iron was found to be a suitable catalyst in combination with methane as the carbon source. It should be pointed out that the catalyst remains in the material after growth, typically 1–2 wt%, and, if necessary should be eliminated in a subsequent step. The process resulted in the formation of nanotubes and nanofibres inside the confined porosity. Their organization depends on the distribution of catalyst particle size and shape. Nanofibres bundle around the larger catalyst particles with multi-wall CNTs growing into the pores. No growth could be obtained using a nickel catalyst. Within our experimental conditions ethanol or water did not have an enhancer effect. Our analyses indicate that pore sizes and flow rates play a determining role. Slower flow favours growth formation and a minimum pore width above 27 μm is needed to enable in situ growth of CNTs and nanofibres inside the scaffold.

Acknowledgements

The authors would like to thank Gary Stakalls and Leroy Grey for technical assistance, a grant from the Army Engineer Research and Development Centre International Research Office (contract no: W911NF-10-1-0438), and EPSRC Science and Innovation Grant Building New Capability in Structural Ceramics (EP/F033605/1) for funding, and Dr. Charles R. Welch for comments on the manuscript. RCM is grateful for funding Award No KUK-F1-020-21, made by King Abdullah, University of Science and Technology (KAUST). SB and ES would like to thank the European Commission (FP7 programme) for the funding (Intra-European Marie Curie Fellowship ACIN and reintegration grant BISM). NN would like to thank the UK Engineering and Physical Sciences Research Council for the funding (EPSRC Doctoral Prize Fellowship).

References

1. Baughman RH, Zakhidov AA, De Heer WA. Carbon nanotubes – the route toward applications. *Science* 2002;**297**:787–92.
2. Xia Y, Yang P, Sun Y, Wu Y, Mayers B, Gates B, et al. One-dimensional nanostructures: synthesis, characterization, and applications. *Adv Mater* 2003;**15**:353–89.
3. Cho J, Boccaccini AR, Shaffer MSP. Ceramic matrix composites containing carbon nanotubes. *J Mater Sci* 2009;**44**:1934–51.
4. Cho J, Inam F, Reece MJ, Chlup Z, Dlouhy I, Shaffer MSP, et al. Carbon nanotubes: do they toughen brittle matrices? *J Mater Sci* 2011;**46**:4770–9.
5. Chu BTT, Tobias G, Salzmann CG, Ballesteros B, Grobert N, Todd RI, et al. Fabrication of carbon-nanotube-reinforced glass–ceramic nanocomposites by ultrasonic in situ sol–gel processing. *J Mater Chem* 2008;**18**:5344.
6. Wang X, Padture NP, Tanaka H. Contact-damage-resistant ceramic/single-wall carbon nanotubes and ceramic/graphite composites. *Nat Mater* 2004;**3**:539–44.
7. Zhan G-D, Kuntz JD, Wan J, Mukherjee AK. Single-wall carbon nanotubes as attractive toughening agents in alumina-based nanocomposites. *Nat Mater* 2003;**2**:38–42.
8. Borrell A, Rocha VG, Torrecillas R, Fernández A. Surface coating on carbon nanofibers with alumina precursor by different synthesis routes. *Compos Sci Technol* 2011;**71**:18–22.
9. Flahaut E, Peigney A, Laurent C, Marlière C, Chastel F, Rousset A. Carbon nanotube-metal-oxide nanocomposites: microstructure, electrical conductivity and mechanical properties. *Acta Mater* 2000;**48**:3803–12.
10. Otieno G, Koos AA, Dillon F, Wallwork A, Grobert N, Todd RI. Processing and properties of aligned multi-walled carbon nanotube/aluminoborosilicate glass composites made by sol–gel processing. *Carbon* 2010;**48**:2212–7.
11. Abarrategi A, Gutiérrez MC, Moreno-Vicente C, Hortigüela MJ, Ramos V, López-Lacomba JL, et al. Multiwall carbon nanotube scaffolds for tissue engineering purposes. *Biomaterials* 2008;**29**:94–102.
12. Harrison BS, Atala A. Carbon nanotube applications for tissue engineering. *Biomaterials* 2007;**28**:344–53.
13. McKenzie JL, Waid MC, Shi R, Webster TJ. Decreased functions of astrocytes on carbon nanofiber materials. *Biomaterials* 2004;**25**:1309–17.
14. Chen X, Hong L, Xu Y, Ong ZW. Ceramic pore channels with inducted carbon nanotubes for removing oil from water. *ACS Appl Mater Interfaces* 2012;**4**:1909–18.
15. Gutierrez MC, Hortiguela MJ, Amarilla JM, Jimenez R, Ferrer ML, del-Monte F. Macroporous 3D architectures of self-assembled MWCNT surface decorated with Pt nanoparticles as anodes for a direct methanol fuel cell. *J Phys Chem C* 2007;**111**:5557–60.
16. Mitchell RR, Gallant BM, Thompson CV, Shao-Horn Y. All-carbon-nanofiber electrodes for high-energy rechargeable Li–O_2 batteries. *Energy Environ Sci* 2011;**4**:2952.
17. Menner A, Verdejo R, Shaffer M, Bismarck A. Particle-stabilized surfactant-free medium internal phase emulsions as templates for porous nanocomposite materials: poly-pickering-foams. *Langmuir* 2007;**23**:2398–403.
18. Boccaccini AR, Cho J, Roether JA, Thomas BJC, Jane Minay E. Shaffer MSP. Electrophoretic deposition of carbon nanotubes. *Carbon* 2006;**44**:3149–60.
19. Aryal S, Kim CK, Kim K-W, Khil MS, Kim HY. Multi-walled carbon nanotubes/TiO_2 composite nanofiber by electrospinning. *Mater Sci Eng C* 2008;**28**:75–9.
20. Rul S, Laurent C, Peigney A, Rousset A. Carbon nanotubes prepared in situ in a cellular ceramic by the gelcasting-foam method. *J Eur Ceram Soc* 2003;**23**:1233–41.
21. Cordier A, Flahaut E, Viazzi C, Laurent C, Peigney A. In situ CCVD synthesis of carbon nanotubes within commercial ceramic foam. *J Mater Chem* 2005;**15**:4041.
22. Cordier A, Rossignol F, Laurent C, Chartier T, Peigney A. A new fast method for ceramic foam impregnation: application to the CCVD synthesis of carbon nanotubes. *Appl Catal A* 2007;**319**:7–13.
23. Du H-B, Li Y-L, Zhou F-Q, Su D, Hou F. One-step fabrication of ceramic and carbon nanotube (CNT) composites by in situ growth of CNTs. *J Am Ceram Soc* 2010;**93**(5):1290–6.
24. Deville S, Saiz E, Tomsia AP. Ice-templated porous alumina structures. *Acta Mater* 2007;**55**:1965–74.
25. Yamamoto N, John Hart A, Garcia EJ, Wicks SS, Duong HM, Slocum AH, et al. High-yield growth and morphology control of aligned carbon nanotubes on ceramic fibers for multifunctional enhancement of structural composites. *Carbon* 2009;**47**:551–60.
26. Deville S, Saiz E, Nalla RK, Tomsia AP. Freezing as a path to build complex composites. *Science* 2006;**311**:515–8.
27. Waschkies T, Oberacker R, Hoffmann MJ. Investigation of structure formation during freeze-casting from very slow to very fast solidification velocities. *Acta Mater* 2011;**59**:5135–45.
28. Deville S. Freeze-casting of porous ceramics: a review of current achievements and issues. *Adv Eng Mater* 2008;**10**:155–69.
29. Butler MF, Instability Formation. Directional Dendritic Growth of Ice Studied by Optical Interferometry. *Cryst Growth Des* 2001;**1**:213–23.
30. Zhang H, Hussain I, Brust M, Butler MF, Rannard SP, Cooper AI. Aligned two- and three-dimensional structures by directional freezing of polymers and nanoparticles. *Nat Mater* 2005;**4**:787–93.
31. Kapilashrami E, Jakobsson A, Seetharaman S, Lahiri AK. Studies of the wetting characteristics of liquid iron on dense alumina by the X-ray sessile drop technique. *Metall Mater Trans B* 2003;**34**:193–9.
32. Lambert JM, Ajayan PM, Bernier P, Planeix JM, Brotons V, Coq B, et al. Improving conditions towards isolating single-shell carbon nanotubes. *Chem Phys Lett* 1994;**226**:364–71.
33. Andrews R, Jacques D, Qian D, Dickey EC. Purification and structural annealing of multiwalled carbon nanotubes at graphitization temperatures. *Carbon* 2001;**39**:1681–7.

34. Xu Y-Q, Peng H, Hauge RH, Smalley RE. Controlled multistep purification of single-walled carbon nanotubes. *Nano Lett* 2005;**5**: 163–8.
35. Amelinckx S, Zhang XB, Bernaerts D, Zhang XF, Ivanov V, Nagy JB. A formation mechanism for catalytically grown helix-shaped graphite nanotubes. *Science* 1994;**265**:635–9.
36. Rodriguez NM. A review of catalytically grown carbon nanofibers. *J Mater Res* 1993;**8**:3233–50.
37. Chhowalla M, Teo KBK, Ducati C, Rupesinghe NL, Amaratunga GAJ, Ferrari AC, et al. Growth process conditions of vertically aligned carbon nanotubes using plasma enhanced chemical vapor deposition. *J Appl Phys* 2001;**90**:5308.
38. Futaba DN, Goto J, Yasuda S, Yamada T, Yumura M, Hata K. General rules governing the highly efficient growth of carbon nanotubes. *Adv Mater* 2009;**21**:4811–5.
39. Hata K, Futaba DN, Mizuno K, Namai T, Yumura M, Iijima S. Water-assisted highly efficient synthesis of impurity-free single-walled carbon nanotubes. *Science* 2004;**306**:1362–4.
40. Amama PB, Pint CL, McJilton L, Kim SM, Stach EA, Murray PT, et al. Role of water in super growth of single-walled carbon nanotube carpets. *Nano Lett* 2009;**9**:44–9.
41. Zhang Y, Gregoire JM, Van Dover RB, Hart AJ. Ethanol-promoted high-yield growth of few-walled carbon nanotubes. *J Phys Chem C* 2010;**114**:6389–95.